Progress in Natural Science: Materials International xxx (xxxx) xxx

HOSTED BY

ELSEVIER

Contents lists available at ScienceDirect

Progress in Natural Science: Materials International

journal homepage: www.elsevier.com/locate/pnsmi

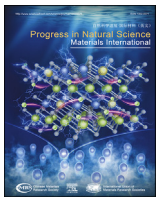

Ultrafast synthesis of highly graphitized carbon foams through water explosion method

Pengfei Huang [a,b], Zhikai Miao [b], Zekun Li [b], Li Chen [b], Yuan Li [b], Zhedong Liu [b], Jingchao Zhang [b], Jiawei Luo [b], Wenjun Zhang [a], Wei-Di Liu [c], Xinxi Zhang [a], Rongtao Zhu [a,**], Yanan Chen [b,*]

[a] School of Chemical Engineering and Technology, China University of Mining and Technology, Xuzhou, 221116, Jiangsu, China
[b] School of Materials Science and Engineering, Key Laboratory of Advanced Ceramics, Machining Technology of Ministry of Education, Tianjin Key Laboratory of Composite and Functional Materials, Tianjin University, Tianjin, 300072, China
[c] School of Chemistry and Physics, ARC Research Hub in Zero-emission Power Generation for Carbon Neutrality, and Centre for Materials Science, Queensland University of Technology, Brisbane, 4000, Australia

ARTICLE INFO

Keywords:
Water explosion
Joule heating
Carbon foam
High graphitization
Lithium-ion batteries anode

ABSTRACT

In recent years, carbon foams have attracted considerable attention due to their distinctive physical and chemical properties, including high specific surface area, excellent electrical conductivity, and robust chemical stability, which render them highly suitable for applications in energy storage, catalysis, and adsorption. However, conventional carbon foams are limited by low levels of graphitization and a lack of long-range structural order, restricting their use in high-performance applications. Traditional synthesis methods, such as templating, chemical activation, and hydrothermal processes, although effective in forming porous structures, are complex and inefficient. To overcome these limitations, this study introduces a novel one-step water explosion method that combines Joule heating and steam activation to synthesize highly graphitized porous carbon foam. By rapidly vaporizing intercalated water molecules between graphite layers, the method overcomes van der Waals forces, leading to the exfoliation of the material. The process, conducted under ultra-high temperatures in less than 1 s, produces carbon foam with high porosity, large surface area, and excellent electrochemical performance. In lithium-ion battery tests, the carbon foam exhibited a high capacity of 516.2 mAh/g at 0.1 A/g and retained 92.77 % of its capacity after 1100 cycles. This efficient and scalable synthesis technique offers a promising pathway for the development of advanced anode materials in energy storage applications, significantly outperforming conventional graphite-based materials.

1. Introduction

In recent years, carbon foams [1,2] have attracted significant research attention due to their unique physical and chemical properties, such as high specific surface area [3], excellent electrical conductivity [4], and strong chemical stability. These characteristics make them highly suitable for applications in energy storage [5,6], catalysis [7], and adsorption [8], including lithium-ion batteries [9], capacitors, catalyst supports, and gas adsorption. However, conventional carbon foams often suffer from a low degree of graphitization and a lack of long-range structural order [10], limiting their performance in applications that require high electrical conductivity and mechanical strength. Numerous synthesis methods have been explored for producing carbon foams [11], such as templating techniques [12], activation strategies [13], and hydrothermal processes [14], have been developed.

Despite their advantages, these methods also exhibit several notable limitations. The template method, for instance, is capable of precisely controlling the pore structure by etching or removing a sacrificial template [15]. However, this process is often complex, involving multiple steps that hinder large-scale production [16]. Chemical activation [17], another widely used method, achieves high porosity through the reaction of chemical agents with carbon precursors, but it typically requires large amounts of environmentally hazardous chemicals, which is inconsistent with the principles of green chemistry. In contrast, physical activation

* Corresponding author.
** Corresponding author.
E-mail addresses: rtzhu2010@cumt.edu.cn (R. Zhu), yananchen@tju.edu.cn (Y. Chen).

https://doi.org/10.1016/j.pnsc.2024.10.001
Received 20 September 2024; Received in revised form 29 September 2024; Accepted 1 October 2024

methods [18], which use carbon dioxide or steam as activating agents, do not require harmful chemicals but are limited by long reaction times and low efficiency. The hydrothermal method [19], which relies on high-temperature, high-pressure reactions between organic precursors or carbon sources, can produce carbon foams, but the resulting low degree of graphitization, which restricts both electrical conductivity and mechanical strength [20].

To overcome these challenges, Joule heating [21] has emerged as a promising technique. Joule heating converts electrical energy into heat through resistive heating as current flows through a material [22]. This method offers rapid heating and precise temperature control, allowing for the efficient processing and modification of materials in a very short time [23]. However, conventional Joule heating is not typically suited for the direct synthesis of porous materials, limiting its broader application in porous carbon production [24].

In this study, we developed a novel one-step process based on water explosion technology, combining Joule heating with steam activation to transform graphite sheets into carbon foam. In this method, water molecules intercalated between graphite layers are rapidly vaporized at high temperatures, overcoming the van der Waals forces [25,26] between layers and causing exfoliation. The application of ultra-high temperatures in an extremely short time, alongside a small amount of steam, prevents the destruction of in-plane carbon-carbon bonds in the graphite sheets, thereby preserving the in-plane structure while producing a highly graphitized porous material. Compared to traditional methods, this process not only simplifies synthesis but also achieves ultra-fast production within 1 s without the use of any toxic chemical agents. The resulting porous carbon foam exhibits a high porosity, large specific surface area, and excellent electrochemical performance. In lithium-ion battery tests, the material achieved a high capacity of 516.2 mAh/g at 0.1 A/g, and after 1100 cycles, it retained 92.77 % of its capacity, significantly exceeding the theoretical capacity of conventional graphite. This efficient and scalable method offers a new pathway for the developing advanced anode materials for energy storage applications, presenting promising potential for the next generation of high-performance lithium-ion batteries.

2. Results and discussion

2.1. Joule heating process

A schematic diagram of a flash Joule heating device is shown in Fig. 1a. Graphite sheets, as depicted in Fig. S1a (5 cm*1 cm), were placed between copper electrodes and connected to a 6 mF capacitor via wires. In order to gain a gain a deeper understanding of the temporal evolution of temperature distribution in graphene sheets during capacitor discharge Joule heating, infrared temperature measurement techniques were employed for temperature signal acquisition and analysis (Fig. 1b) [27]. As the voltage increases, the temperature of the sample also rises, eventually peaking at 3000K, with discharge durations typically remaining within 1 s. The inset image displays the discharge process of the graphite sheet when the capacitor voltage reaches 80V, and an optical photo of the graphite sheet after Joule heat treatment (Figure S1 b). As illustrated in Figure S2 (a–c), graphite sheets of varying thicknesses (20, 50, and 200 μm) underwent water immersion treatment before being subjected to Joule heat treatment. Notably, the initial 200-μm-thick

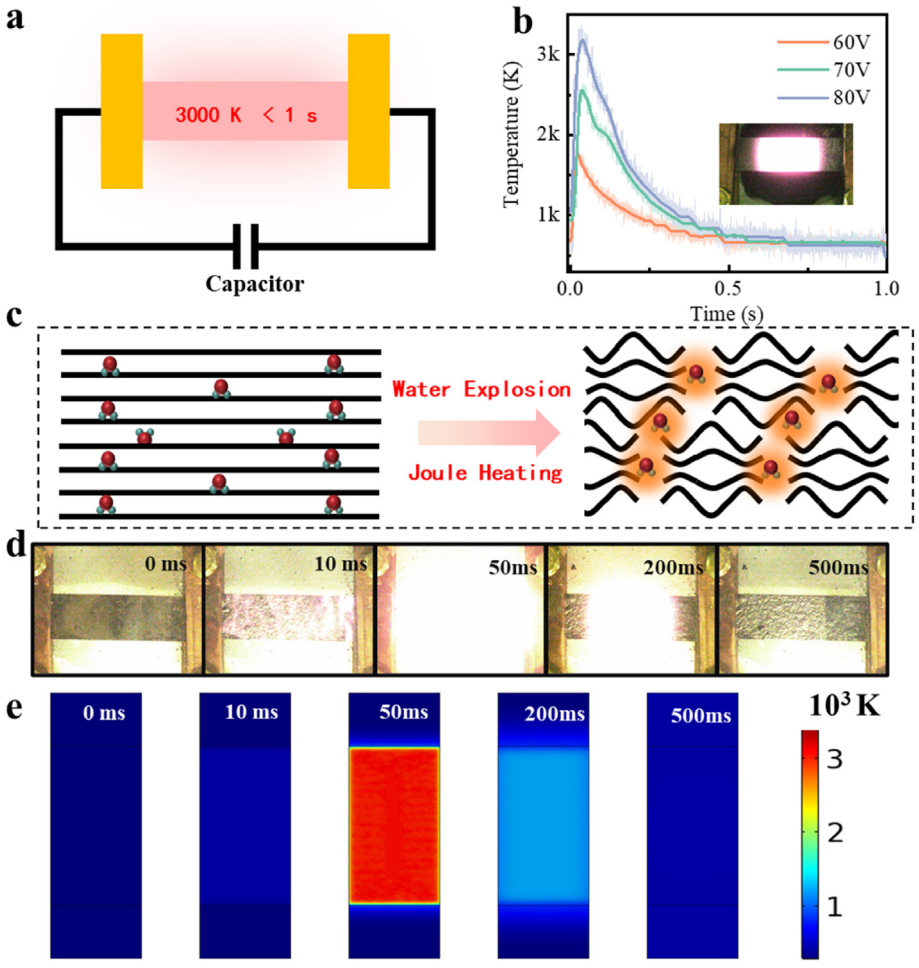

Fig. 1. (a) Schematic diagram of a flash Joule heating device used for treating graphite sheets. (b) Infrared temperature measurements during the capacitor discharge at different voltages (60V, 70V, 80V). Inset: Optical image of the graphite sheet during Joule heating at 80V. (c) Schematic representation of water explosion and Joule heating processes in graphite sheets. (d) High-speed camera images showing the evolution of brightness on the graphite surface during capacitor discharge at 0 ms, 10 ms, 50 ms, 200 ms, and 500 ms. (e) COMSOL Multiphysics simulation results of temperature distribution across the graphite sheet during capacitor discharge.

graphite sheets underwent a remarkable transformation, resulting in the formation of 1-cm-thick carbon foam with a 50-fold increase in volume. In contrast, for graphite sheets that hadn't undergone the water immersion treatment (Figure S1 b), only surface protrusions were observable, and there was no significant change in volume. Furthermore, Fig. 1b presents an optical photograph of the sample resting on a feather after Joule heating, vividly showcasing the lightweight characteristics of the processed carbon foam.

As depicted in Fig. 1c, the water explosion process exhibits a certain level of complexity. During the water immersion treatment, water molecules permeate the spaces between the graphite layers, particularly concentrating at the ends and surfaces of these layers. When an electric potential is applied across a graphite sheet, Joule heating occurs within the sheet due to its inherent internal resistance, as described by the simple equation $Q = I^2Rt$. In this equation, Q signifies the generation of heat energy, I represents the current, R denotes the sheet resistance, and t represents the time involved. It is within this meticulously controlled environment that the graphite sheets undergo a remarkable transformation. Upon heating, intercalated water molecules vaporize, releasing energy that induces bending and expansion of graphite layers. In this intricately orchestrated interplay of electricity, water, and a carbonaceous matrix, the final outcome is the mesmerizing creation of carbon foam.

To gain deeper insights into the temperature dynamics and reaction mechanisms during Joule heating, we employed high-speed camera recordings and COMSOL Multiphysics simulations. These tools enabled precise tracking of temperature distribution and helped validate the uniform heating observed in our experiments. High-speed camera results show that within the first 10 ms of the discharge, bright spots begin to appear on the surface of the graphene sheet (Fig. 1d). At 50 ms, the light intensity reaches the peak and the sample temperature reaches 3000K. At 500 ms, the light emission stops and the temperature drops below 1000K, which is consistent with the temperature curve in Fig. 1b. The capacitor discharge process triggers extreme Joule heat, rapidly raising the temperature to 3000K in a very short time (1 s), further highlighting the high efficiency and high-temperature characteristics of the Joule heat reaction in material preparation. The COMSOL Multiphysics software was used to perform electrothermal simulation, and the temperature distribution of graphite sheets during capacitor discharge was successfully simulated. The simulation results show that during the Joule heating process (Fig. 1 e), the temperature distribution of graphite sheets shows very uniform characteristics. This is due to the in-situ generation of heat within the graphite sheet by Joule heating, achieving overall temperature equilibrium. Additionally, the graphite sheet effectively conducts heat during the Joule heating process, thus avoiding temperature concentration and the formation of hotspots. However, traditional heating methods (radiation, convection, conduction, etc.) inevitably lead to the formation of temperature gradients due to complex heat transfer processes [28]. This is of great significance for the stability of materials in high-temperature environments and the control of the preparation process [29].

2.2. Structural characterization

Through X-ray diffraction (XRD) analysis, the structural changes of graphite samples after Joule heat treatment and water explosion treatments can be studied (Fig. 2 a). After Joule heat treatment, it was observed that the d_{002} peak in the XRD pattern of the graphite sample shifted to a lower angle. This shift indicates an increase in the spacing between graphite layers. After water explosion treatments, the d_{002} peak in the XRD pattern further shifted, and the originally sharp diffraction peak also broadened significantly [30]. These phenomena imply the rearrangement and change of the graphite interlayer structure. Under the combined action of water explosion treatments and Joule heat treatment, the graphite layers are rearranged and changed. This rearrangement involves the local movement of graphite molecules, deformation between layers, and the formation of new structures. The interlayer spacing is

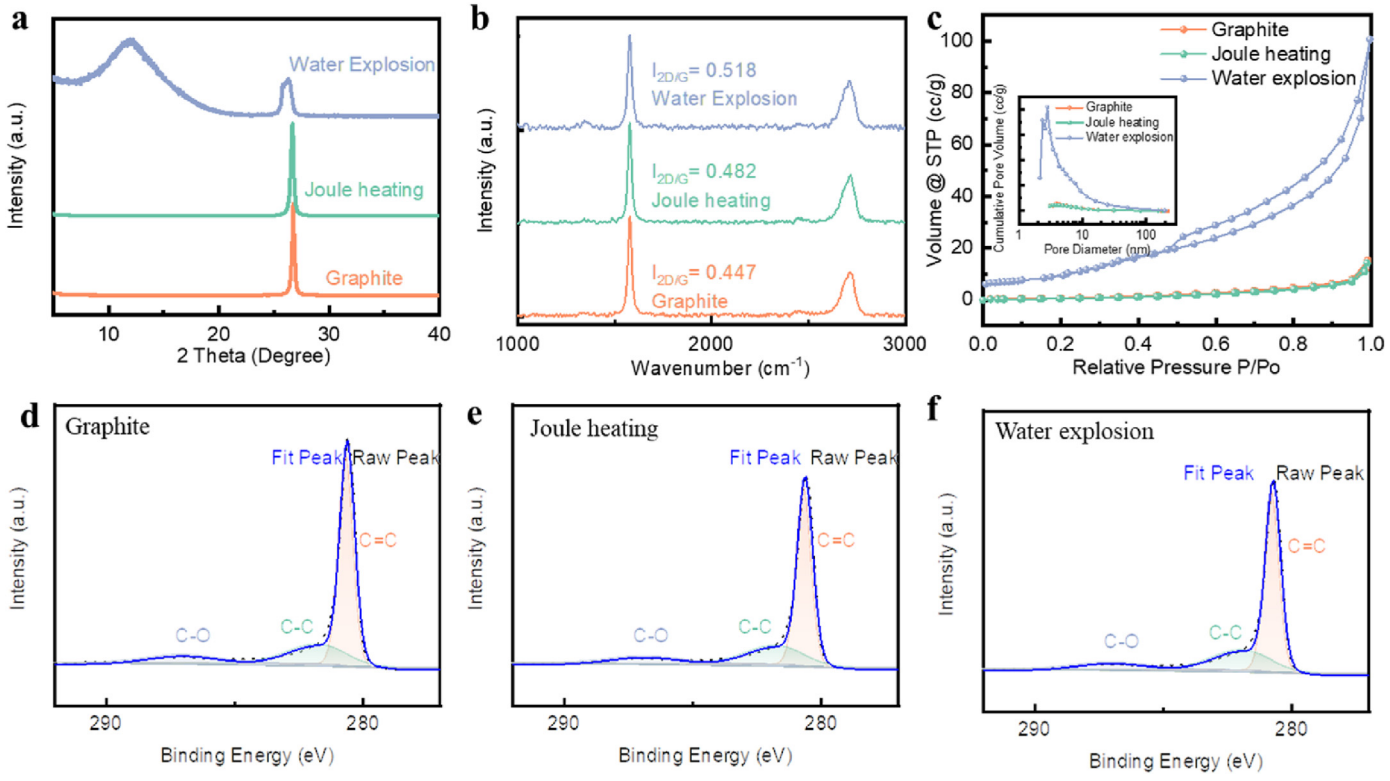

Fig. 2. Comparative analysis of graphite, Joule heating, and water explosion treatments. (b) X-ray diffraction (XRD) patterns; (c) Raman spectra; (d) Nitrogen adsorption-desorption isotherms with pore size distribution inset; (e–g) X-ray photoelectron spectroscopy (XPS) spectra of C1s for graphite, Joule heating, and water explosion samples, respectively.

0.40 nm, which greatly increases the interlayer spacing and reduces the interlayer van der Waals force.

The Raman spectrum results of the treated graphite sample show (Fig. 2 b) that the G peaks [31] are not obviously observed, indicating that there is a lack of obvious lattice defect structure in the sample; while the 2D peaks are enhanced, suggesting that the graphite during the treatment The interlayer spacing of the sheets is increased, and the chaotic stratified arrangement of the graphite sheets is also improved. This result shows that the treatment did not seriously damage the in-plane structure of graphite, but induced microscopic changes in the interlayer structure while maintaining its overall integrity, which provides in-depth insights into the impact on the conductivity and other properties of graphite samples. The results of BET (Brunauer-Emmett--Teller) [32] surface area analysis show (Fig. 2 c and Table 1) that the pores of the treated sample increased significantly, which means that the specific surface area of the sample increased. This increased pore structure provides more channels and surface area for the transport of ions in the electrolyte, helping to increase the ion diffusion rate of the material in the electrolyte. This is of great significance for the material's charge and discharge performance and rapid ion transport in applications such as batteries.

From a chemical bond perspective, Fig. 2d–f illustrates the changes in the C1s peak [33] of graphite samples after Joule heating and water explosion treatments. In the untreated graphite sample (Fig. 2 d), the C1s peak displays typical C=C (carbon-carbon double bond) and C-C (carbon-carbon single bond), characteristic of sp^2 hybridized carbon materials, indicating a complete layered structure and low oxidation. After Joule heating (Fig. 2 e), the C=C and C-C bonds remain dominant, with no significant C-O (carbon-oxygen) bonds observed. This suggests that Joule heating primarily affects the physical form of the graphite without introducing notable chemical changes, preserving the stability of the internal layered structure and preventing oxidation. For the water explosion-treated sample (Fig. 2 f), despite the intense process and noticeable interlayer expansion, the extremely short duration (about 1 s) and limited amount of water vapor do not provide sufficient time or conditions for new C-O bonds to form. Consequently, the XPS analysis shows no significant increase in C-O bonds. This indicates that while the water explosion greatly affects the physical structure, it does not lead to oxidation or C-O bond formation due to the brief reaction time and limited steam exposure.

In summary, neither Joule heating nor water explosion treatment significantly alters the chemical bond structure of graphite. In particular, the water explosion process, due to its ultra-short duration and limited water vapor, does not introduce noticeable C-O bonds. This helps maintain the core chemical properties of graphite, which is crucial for its long-term stability in energy storage applications.

Further SEM analysis provided insights into the surface structural changes of the graphite sheet after Joule heat treatment. The original graphite sheet exhibited relatively flat features, a dense structure, and a smooth surface (Fig. 3a–d). However, fine cracks were visible on the sample's surface due to the stacking of graphite sheets. After Joule heat treatment (Fig. 3b–e), numerous holes with a diameter of approximately 500 nm appeared within some of these originally formed cracks caused by the stacked graphite sheets (Fig. 3 e). These holes were distributed around the cracks and displayed regular shapes. This observation suggests that high-temperature Joule heat treatment triggers localized expansion of the graphite structure and rearrangement of carbon atoms, resulting in hole formation. Under water explosion treatments, the original graphite sheets underwent further exfoliation (Fig. 3c–g). These thinner graphite sheets resulted from the instantaneous release of gas and thermal expansion produced by the water explosion reaction. These structural changes significantly increase the material's surface area and provide additional pathways for ion diffusion, enhancing its electrochemical performance in energy storage applications [34].

Fig. S3 illustrates the morphological changes of 50-micron-thick graphite sheets treated under different voltages (60V, 70V, 80V, and 90V). The scanning electron microscopy (SEM) images at both macroscopic and microscopic levels demonstrate the progressive evolution of the graphite layer structure as the applied voltage increases. At 60V (Figures a–c), the graphite sheet exhibits slight expansion, with the surface retaining a relatively dense, layered structure. The SEM images show minimal delamination between the graphite layers, with only a few visible cracks, indicating that the overall morphology of the graphite remains intact at this voltage. When the voltage is increased to 70V (Figures d–f) and 80V (Figures g–i), the degree of expansion becomes more pronounced. The SEM images reveal a looser layered structure, with the appearance of cracks between the layers and localized areas of delamination. Although the graphite layers start to separate, the overall structure remains relatively stable. Under the highest voltage of 90V (Figures j–l), the graphite sheet undergoes the most dramatic expansion and delamination. The SEM images show that the graphite layers have fully separated, forming numerous pores and fractured regions. The structure becomes highly porous, and the interlayer connections are largely destroyed, leading to a much looser overall configuration. In summary, as the voltage increases, the expansion and delamination of the graphite layers become progressively more pronounced. At higher voltages, particularly at 80V and 90V, the graphite undergoes substantial structural changes, with significant layer separation and pore formation. This increased porosity and expansion could enhance the specific surface area and activity of the graphite, making it more suitable for applications such as energy storage and catalysis [35].

Fig. 4 presents high-resolution transmission electron microscopy (TEM) analysis of the structural changes in graphite sheet following Joule heating and water explosion treatments. After Joule heating (Fig. 4a), the graphite sheet exhibits a densely packed layered structure with an interlayer spacing of approximately 0.338 nm (Fig. 4d). This value aligns with X-ray diffraction (XRD) data, confirming that the Joule heating process preserves the typical graphite-layer structure without significantly altering the interlayer spacing. The magnified view in Fig. 4b further illustrates the multilayer graphite arrangement, indicating that Joule heating primarily affects the surface morphology (as confirmed by scanning electron microscopy), without substantially compromising the compactness of the internal layered structure. The selected area electron diffraction (SAED) pattern in Fig. 4c reveals the crystal structure of graphite, supporting the minimal structural disruption caused by Joule heating [36].

In contrast, the structural changes induced by water explosion treatment are more pronounced (Fig. 4e). The TEM images of carbon foams after water explosion treatment reveal a significantly expanded interlayer spacing (Fig. 4g and h), suggesting a transition from multilayer graphite to few-layer graphite. This transition is driven by the rapid vaporization of water trapped between the graphite layers, which results in substantial expansion and exfoliation of the graphite structure. The diffraction ring inset in Fig. 4e further confirms the presence of few-layer

Table 1
Surface area, pore volume, and pore diameter comparison for raw graphite, Joule heating-treated graphite, and water explosion-treated graphite.

	Surface Area			Pore Volume	Pore Diameter	
	BJH adsorption (m^2/g)	BJH desorption (m^2/g)	BJH adsorption (cm^3/g)	BJH desorption (cm^3/g)	BJH adsorption (nm)	BJH desorption (nm)
Raw graphite	6.622	6.719	0.025	0.025	3.852	3.799
Joule heating	6.149	6.166	0.023	0.023	3.846	3.798
Water Explosion	93.678	121.205	0.264	0.276	11.253	9.111

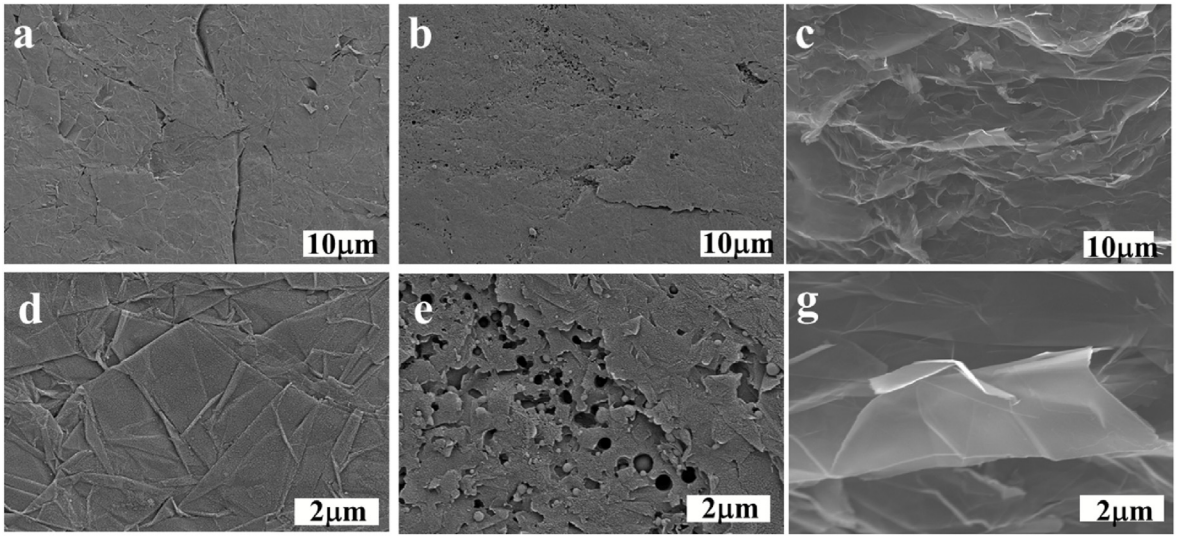

Fig. 3. Morphological analysis of graphite sheet before and after Joule heating and water explosion treatments. (a, d) SEM images of the original graphite sheet; (b, e) SEM images of graphite sheet after Joule heating; (c, f) SEM images of graphite sheet after water explosion.

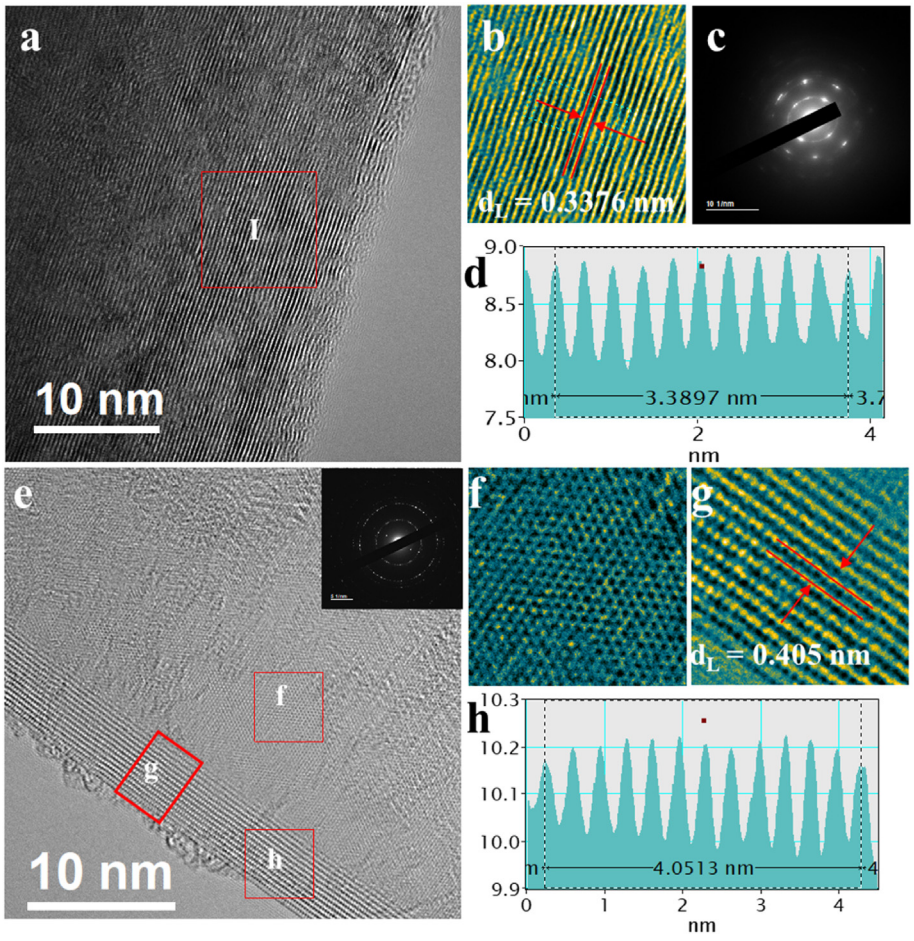

Fig. 4. High-resolution TEM characterization of graphite sheet after Joule heating and water explosion treatments. (a) TEM image of graphite sheet after Joule heating. (b) Magnified TEM image of the selected region. (c) Selected area electron diffraction (SAED) pattern. (d) Corresponding line intensity profile. (e) TEM image of graphite sheet after water explosion treatment, with an inset showing the diffraction pattern. (f) Magnified TEM image of the selected region. (g) Lattice structure of the magnified region. (h) Corresponding line intensity profile.

graphite following the water explosion treatment. Moreover, the magnified image in Fig. 4f shows that despite the expansion and exfoliation caused by water explosion, the surface structure of the graphite remains relatively intact, with no evident damage to the graphene layers.

In summary, Joule heating and water explosion treatments produce distinct effects on the graphite layer structure. Joule heating primarily impacts the surface morphology without notably altering the internal interlayer spacing, whereas water explosion treatment leads to a significant increase in interlayer spacing and a reduction in the number of layers, while maintaining the graphite's structural integrity. The carbon foams formed by water explosion may enhance the material's specific surface area and reactivity, potentially improving its performance in

applications such as energy storage and catalysis [37].

2.3. Molecular dynamics simulation

Molecular dynamics simulations further explain why the graphite structure remains intact after water explosion. The molecular dynamics simulations conducted using LAMMPS [38,39], as illustrated in Fig. 5, provide critical insights into the defect repair mechanisms in graphene sheets subjected to high-temperature conditions. The simulations focus on three distinct types of defects—point defects, pore defects, and line defects—within single-layer graphene. The simulation temperature was set to 4000K to emulate extreme thermal environments, allowing for a detailed observation of defect healing processes.

Fig. 5a–d demonstrate the behavior of point defects, where 5 % of the carbon atoms were randomly removed to simulate atomic vacancies in the graphene lattice. In the initial configuration (Fig. 5b), these vacancies disrupt the six-membered ring structure typical of pristine graphene, creating localized regions of disorder. Upon heating to 4000K, the enhanced mobility of carbon atoms, particularly free radicals, enables them to migrate toward the defective sites. As shown in Fig. 5c and d, the graphene structure undergoes substantial recovery, with most of the vacancies filled by migrating carbon atoms. This suggests that at elevated temperatures, graphene exhibits a strong self-healing capability, efficiently repairing even a high density of point defects. The nearly complete restoration of the hexagonal lattice structure highlights the material's ability to recover its integrity through localized atomic rearrangements driven by thermal energy.

For pore defects, shown in Fig. 5e–h, larger holes were created by removing multiple carbon atoms. Initially, these defects formed substantial voids in the graphene lattice (Fig. 5f). After the application of high-temperature treatment, the pore defects also exhibited full repair (Fig. 5g and h). The mobility of carbon atoms around the defect site facilitated the closure of the holes, as carbon atoms moved to fill the empty spaces. The simulation results reveal that even larger defects, such as pores, were successfully healed, with the graphene sheet returning to its original state. The line defects, depicted in Fig. 5i–l, were the most extended form of disruption simulated. These defects, which created long, continuous gaps in the graphene sheet (Fig. 5j), presented a significant challenge for repair. Despite this, high-temperature treatment led to the complete closure of these line defects as well (Fig. 5k and l). The carbon atoms from both sides of the defect migrated towards the gap, restoring the continuity of the graphene lattice. By the end of the simulation, the line defects were no longer observable, and the graphene structure was fully restored, indicating the effectiveness of high-temperature treatment in repairing even the most complex defects.

In summary, the results of these simulations clearly demonstrate that all types of defects—point, pore, and line—were fully repaired under the simulated high-temperature conditions of 4000K. The enhanced mobility of carbon atoms at elevated temperatures enabled the migration of free radicals and surrounding atoms to defective regions, leading to complete structural recovery. The molecular dynamics simulations demonstrate the self-healing capability of carbon defects at high temperatures, which

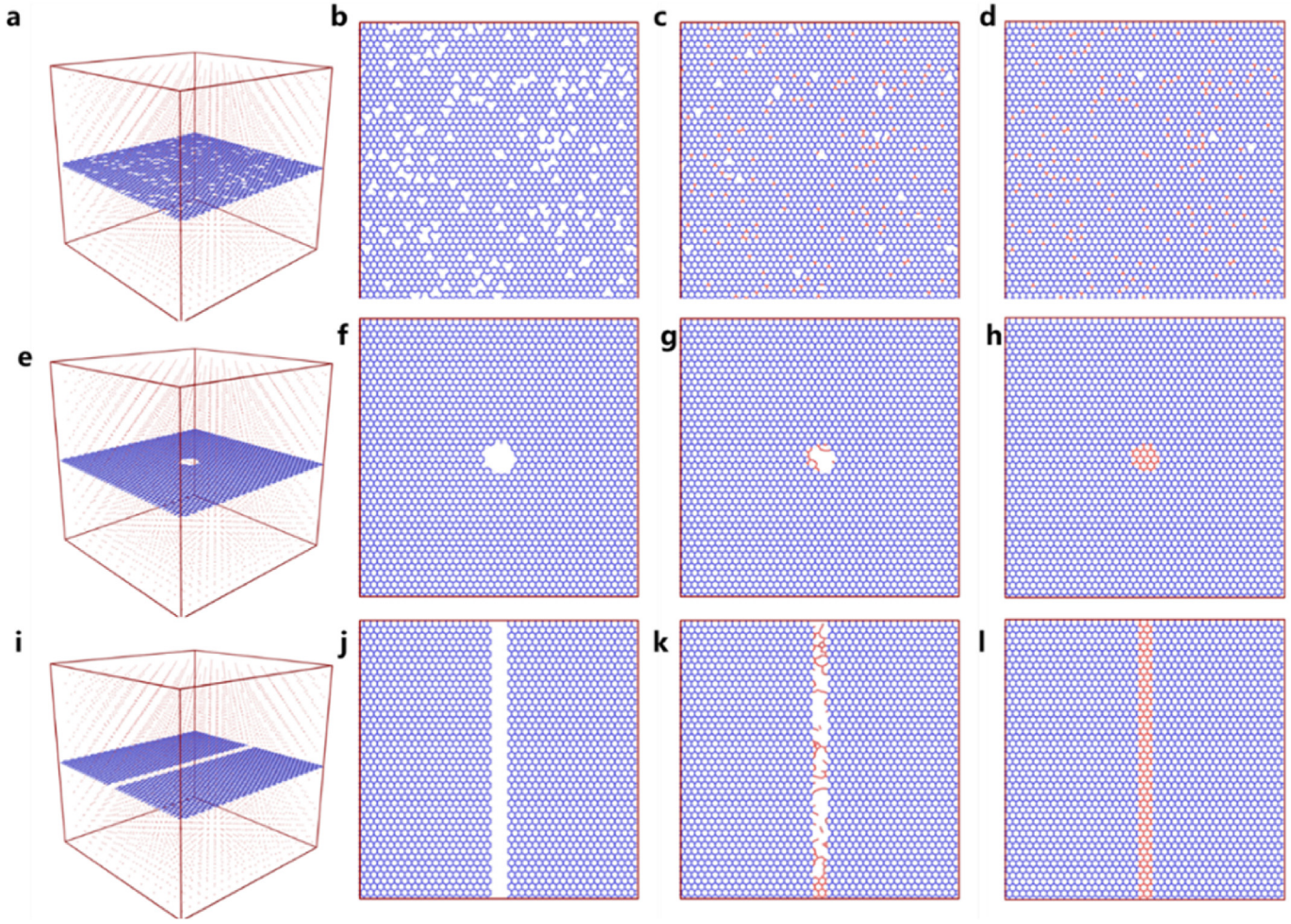

Fig. 5. Structural evolution of three different defect types—point defects, pore defects, and line defects—before and after high-temperature treatment. (a–d) Point defects; (e–h) Pore defects; (i–l) Line defects. In all cases, high-temperature treatment leads to significant repair of the defected structures, as observed by the restoration of the atomic lattice.

directly correlates with the enhanced graphitization observed in the Joule heating process. This structural repair is essential for maintaining the material's high electrical conductivity and long-term stability.

2.4. Electrochemical performance

The electrochemical performance of the prepared porous carbon foam electrode was analyzed in detail. Fig. 6a presents the charge and discharge curves at various current densities (ranging from 0.1 A/g to 5 A/g). At a current density of 0.1 A/g, the initial charge capacity of the material reached 516.2 mAh/g, significantly surpassing the theoretical capacity of graphite (372 mAh/g) [40]. This high capacity is primarily attributed to the material's rich porous structure, which provides additional lithium storage sites and facilitates lithium ion transport, thereby enhancing the efficiency of electrochemical reactions [41]. As a result, at low current densities, the material can fully utilize its high lithium storage capacity. As the current density increases, the charge and discharge capacities gradually decrease. This decline is likely due to the slower diffusion rate of lithium ions at higher current densities, preventing them from fully accessing all the lithium storage sites. Nevertheless, even at higher current densities (such as 5 A/g), the material retains a significant capacity, indicating strong rate performance. Fig. 6b further illustrates the rate cycling performance of the electrode at different current densities. As expected, the capacity decreases noticeably with increasing current density. However, when the current density is restored to the initial 0.1 A/g, the capacity recovers, suggesting that the material's structure remains largely intact even at high current densities, demonstrating high reversibility and structural stability [20]. Fig. 6c shows the results of a long-term cycling test at a fixed current density of 0.2 A/g. After 1100 cycles, the electrode material retains 92.77 % of its initial capacity, indicating exceptional stability during extended cycling. Additionally, the coulombic efficiency remains consistently close to 100 %, confirming the high reversibility of the material and minimal side reactions during the charge-discharge process. The material's extremely high capacity retention rate is attributed to the effective combination of its highly graphitized structure and low defect levels [42]. The Nyquist plot from electrochemical impedance spectroscopy (EIS) (Fig. S4a) reveals the charge transfer resistance and ion diffusion characteristics of the carbon foam electrode in lithium-ion batteries. The galvanostatic intermittent titration technique (GITT) analysis (Fig. S4b) displays the time-dependent potential response alongside the corresponding lithium-ion diffusion coefficient, indicating stable ion transport within the carbon foam during cycling. This combination of long cycle life and high coulombic efficiency underscores the material's great potential for high-capacity energy storage and long-life applications, making it well-suited for practical energy storage devices such as lithium-ion batteries.

Furthermore, Fig. S5 is a schematic diagram of its continuous production. In this continuous process, a graphite sheet is initially fed into a water soaking system, where it absorbs water uniformly across its surface. As the water-saturated graphite sheet advances, it is transferred to the Joule heating stage. The application of electric current heats the sheet rapidly, causing the water to vaporize within the graphite layers. This rapid vaporization leads to the expansion and exfoliation of the graphite, transforming it into a porous carbon foam. The combination of water soaking and Joule heating in a continuous production setup allows for efficient and scalable manufacturing of carbon foams, which are suitable for various applications such as energy storage and thermal management.

3. Conclusion

This study presents a novel and efficient method for synthesizing highly graphitized porous carbon foam using a combination of Joule heating and steam activation through a water explosion process. By exploiting the rapid vaporization of intercalated water molecules between graphite layers, the method achieves exfoliation and structural transformation in an ultra-short time, leading to the formation of a three-dimensional porous structure with enhanced graphitization. The resulting material exhibits excellent electrochemical properties, including high specific capacity and exceptional cycling stability, making it a promising

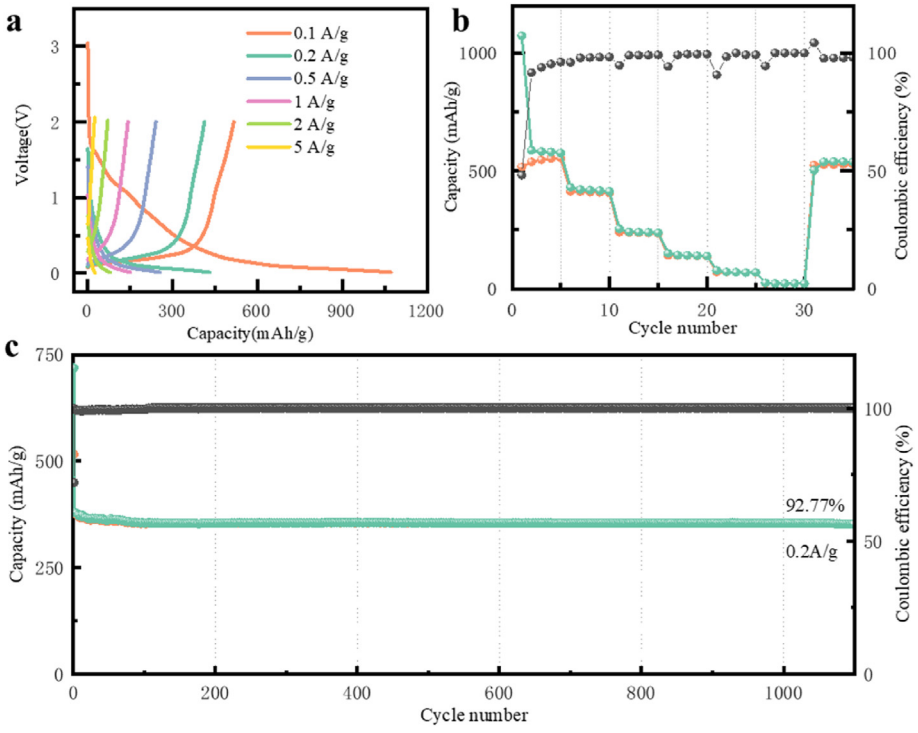

Fig. 6. Electrochemical performance of the carbon foam electrode: (a) Charge and discharge curves at various current densities; (b) rate performance and coulombic efficiency across current densities ranging from 0.1 A/g to 5 A/g; (c) long-term cycling stability at a fixed current density of 0.2 A/g.

candidate for use as an anode material in lithium-ion batteries. In particular, the carbon foam demonstrated a high capacity of 516.2 mAh/g at 0.1 A/g and retained 92.77 % of its capacity after 1100 cycles, far exceeding the theoretical capacity of conventional graphite. Additionally, the method offers significant advantages in terms of simplicity, scalability, and environmental friendliness, as it avoids the use of toxic chemicals and enables ultra-fast synthesis. These findings highlight the potential of this water explosion method for the scalable production of advanced carbon materials, offering broad prospects for energy storage and other high-performance applications.

4. Materials and methods

4.1. Fabrication of carbon foam

The carbon foam was fabricated from commercial graphite sheets measuring 1 cm in width and 5 cm in length with different thicknesses (20, 50, and 200 μm). First, the graphite sheet was soaked in water for 30 s, then removed and securely placed between two electrodes connected to a capacitor (Fig. 1a). Proper alignment and firm placement of the graphite sheet are essential to ensure uniform heating during the capacitor discharge process. The capacitor (6 mF) was connected to a discharge system, with current density and heating duration controlled by adjusting the voltage (60–90V) and discharge time (1 s). When current flows through the graphite sheet, resistive heating rapidly raises its temperature (300K). The sudden temperature rise causes water molecules on or near the graphite surface to evaporate and expand, leading to a rapid increase in local gas pressure. This explosive release of gas, combined with instantaneous heating, induces structural changes in the graphite sheet, forming tiny holes and microcracks on its surface, which eventually results in the formation of carbon foam.

For comparison, a control sample was also prepared by directly subjecting the graphite sheet to Joule heating without prior water immersion, while all other treatment steps remained the same.

4.2. Characterization

The microstructure of the materials was characterized using a MAIA3 LMH scanning electron microscope (SEM) from Tescan USA. The operating voltage was set to 10 kV, and the secondary electron imaging (SEI) mode was employed to observe the pore structure on the sample surface. A JEOL JEM 2100F transmission electron microscope (TEM) was used to obtain high-resolution images of the nanostructure of the samples, with an operating voltage of 200 kV. The crystal structure of the materials was analyzed using selected area electron diffraction (SAED), and high-resolution images were captured to determine the interlayer spacing and microstructural changes. The crystal structure of the materials was studied using a Bruker D-8 Advance X-ray diffractometer (XRD) with a Cu Kα radiation source ($\lambda = 1.54178$ Å). The scanning range was set from 5° to 80°, and the scanning speed was 2°/min. A Senterra Bruker Raman spectrometer with a 532 nm laser wavelength was used to analyze the chemical composition and structural defects of the materials. Raman spectroscopy primarily focused on changes in the D-band and G-band of carbon materials to assess the degree of graphitization and defect density. The chemical bonding structure of the materials was analyzed using a Thermo Scientific ESCALAB 250 X-ray photoelectron spectrometer (XPS). The C1s peak was used for quantitative analysis of features such as carbon-carbon double bonds (C=C) and carbon-oxygen bonds (C-O), allowing for an evaluation of the surface chemical composition and its variations.

4.3. Molecular dynamics simulation

Molecular dynamics simulations were performed using LAMMPS (Large Scale Atomic/Molecular Massively Parallel Simulator), a software tool specialized for simulating molecular dynamics processes. The airebo force field was applied in the simulations, and the results were visualized using OVITO (Open Visualization Tool) version 2.8.2. The cutoff radius for carbon-carbon bonds was set at 1.9 Å. Periodic boundary conditions were used for all simulations, and temperature control was implemented using a Berendsen thermostat.

The simulation process included a time step of 0.5 fs, with heating from 300K to 4000K over 50 ps, followed by 50 ps of constant temperature at 4000K. During the quenching process, the temperature was reduced from 4000K to 3000K over 250 ps, with a cooling rate of 4K/ps, and then cooled further to 300K over 50 ps with a cooling rate of 13.5K/ps. Throughout the simulation, the position of the graphene sheet was fixed to maintain stability during the thermal processes.

4.4. Electrochemical characterization

All electrochemical tests were conducted within CR2032 cells, which were assembled inside a glove box filled with high-purity argon ($H_2O < 0.1$ ppm, $O_2 < 0.1$ ppm). The working electrodes were composed of a mass ratio of 8:1:1 of active material, conductive carbon black, and polyvinylidene fluoride (PVDF). The active mass loading for each electrode was in the range of 1.5–2 mg cm−2. The electrodes were fabricated using pure lithium foil as the current collector, Celgard 2400 polypropylene film as the separator, and a 1.0 M $LiPF_6$ electrolyte solution in a 1:1 vol ratio of ethylene carbonate/diethyl carbonate (EC/DEC). Lithium-ion storage performance were recorded using a NEWARE battery testing system, with a voltage range of 0.01–2.00 V vs. Li+/Li. CHI660E electrochemical workstation (CH Instruments Inc.), used for electrochemical impedance spectroscopy (EIS) measurements.

CRediT authorship contribution statement

Pengfei Huang: Writing – review & editing, Writing – original draft, Visualization, Validation, Methodology, Data curation, Conceptualization. **Zhikai Miao:** Methodology, Formal analysis, Data curation. **Zekun Li:** Methodology, Formal analysis, Data curation. **Li Chen:** Methodology, Formal analysis, Data curation. **Yuan Li:** Methodology, Formal analysis, Data curation. **Zhedong Liu:** Methodology, Formal analysis, Data curation. **Jingchao Zhang:** Methodology, Formal analysis, Data curation. **Jiawei Luo:** Methodology, Formal analysis, Data curation. **Wenjun Zhang:** Writing – original draft, Funding acquisition, Conceptualization. **Wei-Di Liu:** Writing – review & editing, Writing – original draft. **Xinxi Zhang:** Resources, Funding acquisition, Data curation, Conceptualization. **Rongtao Zhu:** Writing – review & editing, Writing – original draft, Resources, Funding acquisition, Formal analysis, Conceptualization. **Yanan Chen:** Writing – review & editing, Writing – original draft, Visualization, Validation, Resources, Funding acquisition, Formal analysis, Data curation, Conceptualization.

Declaration of competing interest

The authors declare that they have no known competing financial interests or personal relationships that could have appeared to influence the work reported in this paper.

Acknowledgements

This work was supported by the National Natural Science Foundation of China (no. 52171219, no. 22109091, U21A20325).

Appendix A. Supplementary data

Supplementary data to this article can be found online at https://doi.org/10.1016/j.pnsc.2024.10.001.

References

[1] B. Chen, D. Wu, T. Wang, F. Yuan, D. Jia, Chem. Eng. J. 462 (2023) 142163.
[2] J. Li, X. Wang, Z. Lin, N. Xu, X. Li, J. Liang, W. Zhao, R. Lin, B. Zhu, G. Liu, L. Zhou, S. Zhu, J. Zhu, Joule 4 (2020) 928–937.
[3] F. Zhang, B. Liu, Z. Ni, X. Zhang, Y. Shao, F. Zhang, K. Sun, R. Fan, D. Jia, Carbon 200 (2022) 281–295.
[4] W. Tian, H. Zhang, X. Duan, H. Sun, G. Shao, S. Wang, Adv. Funct. Mater. 30 (2020) 1909265.
[5] D.S. Priya, L.J. Kennedy, G.T. Anand, Mater. Today Sustainability 21 (2023) 100320.
[6] H. Qiu, L. Zhao, M. Asif, X. Huang, T. Tang, W. Li, T. Zhang, T. Shen, Y. Hou, Energy Environ. Sci. 13 (2020) 571–578.
[7] C. Yang, Y. Wang, M. Liang, Z. Su, X. Liu, H. Fan, T.J. Bandosz, Appl. Catal., B 323 (2023) 122133.
[8] J. Bai, J. Huang, Q. Yu, M. Demir, F.H. Gecit, B.N. Altay, L. Wang, X. Hu, Fuel Process. Technol. 244 (2023) 107700.
[9] Y. Liu, H. Shi, Z.-S. Wu, Energy Environ. Sci. 16 (2023) 4834–4871.
[10] Y. Chen, J. Huang, Z. Chen, C. Shi, H. Yang, Y. Tang, Z. Cen, S. Liu, R. Fu, D. Wu, Adv. Sci. 9 (2022) 2103477.
[11] Z. Guo, X. Han, C. Zhang, S. He, K. Liu, J. Hu, W. Yang, S. Jian, S. Jiang, G. Duan, Chin. Chem. Lett. 35 (2024) 109007.
[12] W. Zhang, R.-r. Cheng, H.-h. Bi, Y.-h. Lu, L.-b. Ma, X.-j. He, N. Carbon Mater. 36 (2021) 69–81.
[13] M. Sevilla, N. Díez, A.B. Fuertes, ChemSusChem 14 (2021) 94–117.
[14] H. Liang, R. Sun, B. Song, Q. Sun, P. Peng, D. She, J. Hazard Mater. 387 (2020) 121987.
[15] T. Zeng, X. Zhu, X. Wang, L. Zhang, Y. Ding, H. Jin, J. Mater. Chem. A 11 (2023) 24712–24723.
[16] C. Wang, B. Yan, J. Zheng, L. Feng, Z. Chen, Q. Zhang, T. Liao, J. Chen, S. Jiang, C. Du, S. He, Adv. Powder Mater. 1 (2022) 100018.
[17] G. Jiang, R.A. Senthil, Y. Sun, T.R. Kumar, J. Pan, J. Power Sources 520 (2022) 230886.
[18] Z. Li, D. Guo, Y. Liu, H. Wang, L. Wang, Chem. Eng. J. 397 (2020) 125418.
[19] Y. Gong, L. Xie, C. Chen, J. Liu, M. Antonietti, Y. Wang, Prog. Mater. Sci. 132 (2023) 101048.
[20] X. Chen, N. Sawut, K. Chen, H. Li, J. Zhang, Z. Wang, M. Yang, G. Tang, X. Ai, H. Yang, Y. Fang, Y. Cao, Energy Environ. Sci. 16 (2023) 4041–4053.
[21] Z. Liu, C. Duan, S. Dou, Q. Yuan, J. Xu, W.-D. Liu, Y. Chen, Small 18 (2022) 2200954.
[22] S. Zhu, F. Zhang, H.-G. Lu, J. Sheng, L. Wang, S.-D. Li, G. Han, Y. Li, ACS Mater. Lett. 4 (2022) 1863–1871.
[23] D.X. Luong, K.V. Bets, W.A. Algozeeb, M.G. Stanford, C. Kittrell, W. Chen, R.V. Salvatierra, M. Ren, E.A. McHugh, P.A. Advincula, Z. Wang, M. Bhatt, H. Guo, V. Mancevski, R. Shahsavari, B.I. Yakobson, J.M. Tour, Nature 577 (2020) 647–651.
[24] P. Huang, Z. Li, L. Chen, Y. Li, Z. Liu, J. Zhang, J. Luo, W. Zhang, W.-D. Liu, X. Zhang, R. Zhu, Y. Chen, ACS Nano 18 (2024) 18344–18354.
[25] X. Gu, S. Hu, C. Zhao, Int. J. Heat Mass Tran. 232 (2024) 125972.
[26] Y. Xia, Y. Xing, M. Li, M. Liu, J. Tan, Y. Cao, X. Gui, Fuel 269 (2020) 117367.
[27] P. Huang, R. Zhu, X. Zhang, W. Zhang, Chem. Eng. J. 450 (2022) 137999.
[28] J.L. Beckham, K.M. Wyss, Y. Xie, E.A. McHugh, J.T. Li, P.A. Advincula, W. Chen, J. Lin, J.M. Tour, Adv. Mater. 34 (2022) 2106506.
[29] W. Chen, J.T. Li, Z. Wang, W.A. Algozeeb, D.X. Luong, C. Kittrell, E.A. McHugh, P.A. Advincula, K.M. Wyss, J.L. Beckham, M.G. Stanford, B. Jiang, J.M. Tour, ACS Nano 15 (2021) 11158–11167.
[30] J. Li, Y. Qin, Y. Chen, J. Shen, Y. Song, Z. Wang, Fuel 333 (2023) 126334.
[31] S. Jovanovic, P. Jakes, S. Merz, R.-A. Eichel, J. Granwehr, Electrochem. Sci. Adv. 2 (2022) e2100068.
[32] Y. Wang, Z. Jin, Energy Fuels 37 (2023) 6601–6609.
[33] B. Rais, E.T. Ostrowski, A. Canton, C.H. Skinner, S. Barison, S. Fiameni, B.E. Koel, Appl. Surf. Sci. 567 (2021) 150830.
[34] C. Lv, C. Lin, X.S. Zhao, eScience 3 (2023) 100179.
[35] B. Jia, B. Zhang, Z. Cai, X. Yang, L. Li, L. Guo, eScience 3 (2023) 100112.
[36] Z. Zhu, Y. Men, W. Zhang, W. Yang, F. Wang, Y. Zhang, Y. Zhang, X. Zeng, J. Xiao, C. Tang, X. Li, Y. Zhang, eScience, 2024 100249.
[37] Y. Yang, M. Tang, Z. Zhang, S. Huang, S. Wu, Nano Res. Energy 2 (2023) e9120065.
[38] A.P. Thompson, H.M. Aktulga, R. Berger, D.S. Bolintineanu, W.M. Brown, P.S. Crozier, P.J. in 't Veld, A. Kohlmeyer, S.G. Moore, T.D. Nguyen, R. Shan, M.J. Stevens, J. Tranchida, C. Trott, S.J. Plimpton, Comput. Phys. Commun. 271 (2022) 108171.
[39] S. Plimpton, J. Comput. Phys. 117 (1995) 1–19.
[40] C. Yang, X. Zhang, J. Li, J. Ma, L. Xu, J. Yang, S. Liu, S. Fang, Y. Li, X. Sun, X. Yang, F. Pan, J. Lu, D. Yu, Electrochim. Acta 346 (2020) 136244.
[41] S. Gao, L. Yan, J. Qin, R. Liu, B. Liang, Q. Wang, M. Geng, B. Wang, J. Mater. Chem. A 11 (2023) 4729–4738.
[42] H.-Y. Lee, C. Gyan-Barimah, C.-H. Shin, J.-S. Yu, J. Mater. Chem. A 11 (2023) 13916–13922.